Induced Seismicity Characterization during Hydraulic-Fracture Monitoring with a Shallow-Wellbore Geophone Array and Broadband Sensors

by David W. Eaton, Nadine Igonin, Andrew Poulin, Ron Weir, Hongliang Zhang, Scott Pellegrino, and German Rodriguez

ABSTRACT

The Tony Creek Dual Microseismic Experiment (ToC2ME) is a field program that used a diverse set of sensors to record a hydraulic-fracturing completion program at a four-well pad west of Fox Creek, Alberta. The acquisition systems consisted of a 68-station shallow borehole array, six broadband seismometers, and one strong-motion accelerometer. This dataset yielded above 4000 events with well-determined magnitudes and hypocenters, with a maximum magnitude of M_w 3.2. The geophones, with a 10-Hz natural frequency, are found to be more suitable for determining event magnitudes below M_w 1.0; seismometers are more suitable above this magnitude. The largest events have strike-slip mechanisms and are clustered above the treatment zone along well-defined north–south lineaments. Several other event clusters are more diffuse and have distinct magnitude characteristics and mechanisms. Horizons extracted from 3D reflection seismic data reveal structural fabrics that are subparallel to event clusters, although the microseismic lineaments do not appear to correlate exactly with seismically imaged features.

Electronic Supplement: Seismicity catalog of 4083 events from the Tony Creek Dual Microseismic Experiment (ToC2ME).

INTRODUCTION

Hydraulic fracturing (HF) is a reservoir-stimulation method wherein fluids are injected under high pressure with the goal of enhancing fluid flow by creating a network of connected fractures (Economides and Nolte, 2000). HF methods are widely used to develop otherwise uneconomic low-permeability unconventional reservoirs (Warpinski *et al.*, 2009). Dense geophone arrays are commonly deployed, either near the surface or in deep wellbores to monitor microseismic activity associated with HF well completions (Warpinski, 2009; Duncan and Eisner, 2010; Van der Baan *et al.*, 2013). In the absence of fault activation, hydraulic fractures generally grow parallel to the horizontal axis of maximum principal stress (S_{Hmax}) and are accompanied by operationally induced microseismicity, which is characterized by magnitudes that are usually less than zero (Maxwell, 2014; Eaton, 2018). Compared with relatively sparse networks of broadband seismometers that are typically used to monitor induced seismicity, dense geophone arrays offer higher spatial resolution and greater sensitivity to low-magnitude events; however, continuous data from HF monitoring datasets collected by industry are not commonly available for scientific research.

The Tony Creek dual Microseismic Experiment (ToC2ME) is a research-focused field program acquired by the University of Calgary from 25 October to 15 December 2016 using a combination of a shallow-borehole geophone array, direct-burial broadband seismometers, and a strong-motion accelerometer (Fig. 1). This diverse set of sensors was used to monitor a four-well HF program within the Kaybob-Duvernay region of Alberta, Canada, where anomalous seismicity induced by HF has been previously documented (Atkinson *et al.*, 2016; Bao and Eaton, 2016; Schultz *et al.*, 2017, 2018). Here, the term *anomalous* is used in reference to seismic events with $M_w > 0$, which do not generally occur during HF operations (Eaton, 2018). During the acquisition of the ToC2ME dataset, several distinct sequences of anomalous-induced earthquakes were recorded, up to a maximum magnitude of M_w 3.2. This dataset provides an unusual opportunity to characterize HF fault-activation processes, including broadband spectra and precise locations of foreshock, mainshock, and aftershock sequences including events that are too weak to be detected with regional networks. Although swarm-like behavior has been documented for HF-induced events (Skoumal *et al.*, 2015), in this study, each seismicity

doi: 10.1785/0220180055

Downloaded from https://pubs.geoscienceworld.org/ssa/srl/article-pdf/89/5/1641/4317066/srl-2018055.1.pdf
by Univ Calgary Library user
on 09 November 2018

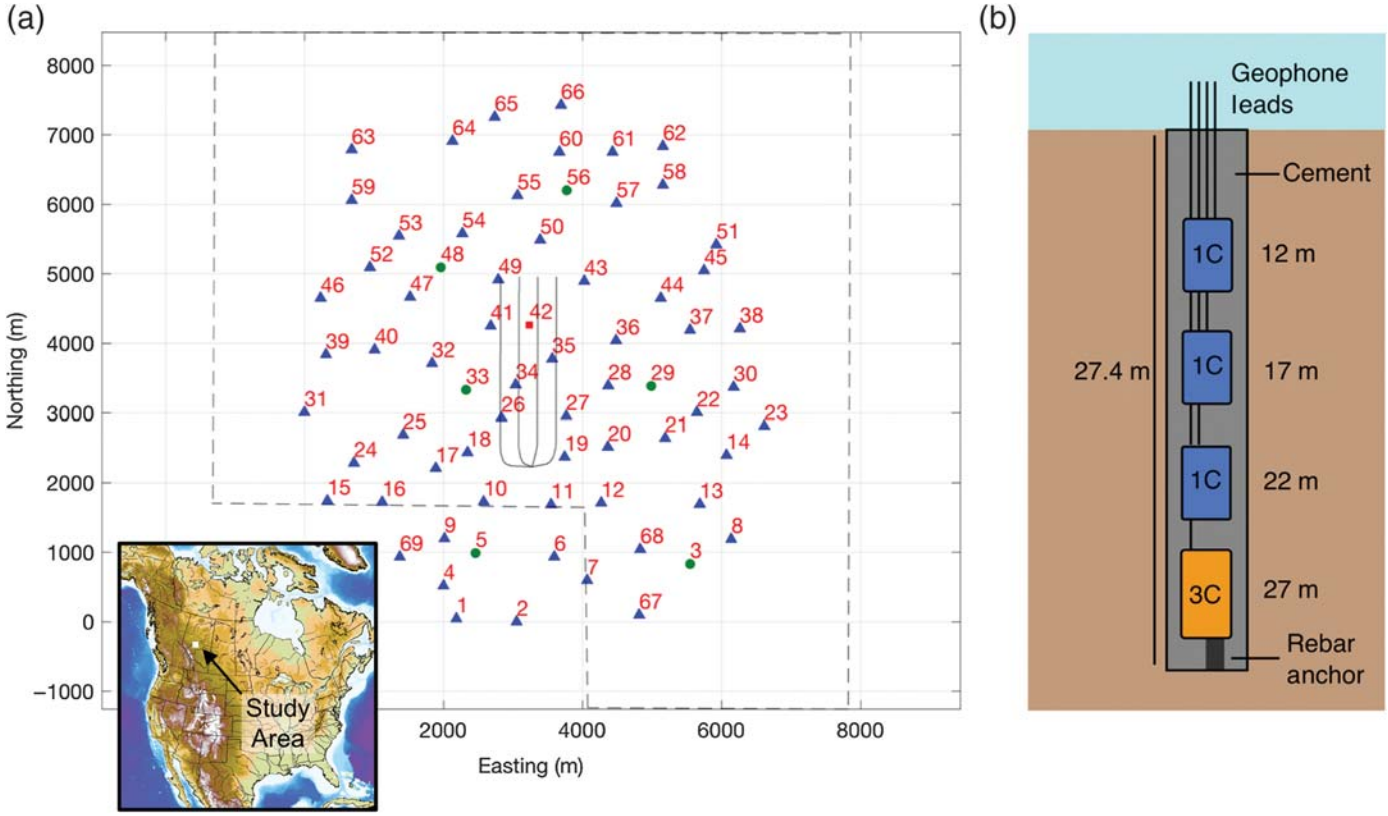

▲ **Figure 1.** (a) Map showing distribution of the Tony Creek Dual Microseismic Experiment recording systems and hydraulic-fracturing (HF) treatment wells. Green circles indicate sites with collocated broadband sensor and shallow borehole array station. The small red square indicates a collocated accelerometer and shallow borehole array station. Blue triangles are shallow borehole stations only. The dashed polygon outlines the extent of 3D seismic data used in this study. Inset shows location of the study area in western Canada. (b) Schematic diagram showing configuration of a shallow borehole geophone array, consisting of a three-component (3C) geophone at 27 m depth and three vertical-component geophones at shallower depths.

cluster contains one (or a few) events with distinctly higher magnitude; the terms *foreshock* and *aftershock* are thus used to provide temporal context for lower magnitude seismicity within each cluster, with respect to these larger events.

The ToC2ME microseismic and induced-seismicity dataset is complemented by 3D multicomponent seismic data from the same area (Weir *et al.*, 2018), as well as nearby deep-crustal seismic data (Eaton *et al.*, 1999; Ekpo *et al.*, 2018), well logs, and cores. Taken together, these various types of data provide exceptional opportunities for integrated geomechanical interpretation. The overall objectives of the ToC2ME program are to improve our understanding of the microseismic and induced-seismicity response to HF within a region of high geological susceptibility to fault activation to elucidate links between seismicity and structural features discernible in 3D seismic data and to test new models for geological susceptibility for induced seismicity (Pawley *et al.*, 2018). This article presents the first results of the ToC2ME initiative and focuses on acquisition and processing of the passive seismic data and joint interpretation of the microseismic event distribution and 3D seismic data.

DATA ACQUISITION

The geometry and borehole-array configuration are shown in Figure 1. The geophones have a natural frequency of 10 Hz, and continuous data were recorded during the HF program using OYO Geospace Seismic Recorder (GSX)-3 systems with a sampling rate of 0.002 s. Geophones were cemented into 68 shallow wellbores at depths from 12 to 27 m. Vertical-component geophones were installed at 12, 17, and 22 m, providing data for characterizing the near surface. At the deepest level (27 m) for each station, a three-component (3C) geophone was installed. The absolute orientations of the two horizontal components of the 3C geophones were unknown before the field program. The broadband seismometers consisted of Trillum Compact sensors. These were buried to a depth of about 1 m and have a flat frequency response from 20 s to 100 Hz. As described later, the use of both types of sensors enabled robust determination of moment magnitude over a range from $M_w - 1$ to 3.2. A Nanometrics Titan strong-motion accelerometer was also deployed, enabling accurate recording of ground acceleration for larger events, for which signals were otherwise clipped for both geophones and broadband seismometers.

Downloaded from https://pubs.geoscienceworld.org/ssa/srl/article-pdf/89/5/1641/4317066/srl-2018055.1.pdf
by Univ Calgary Library user
on 09 November 2018

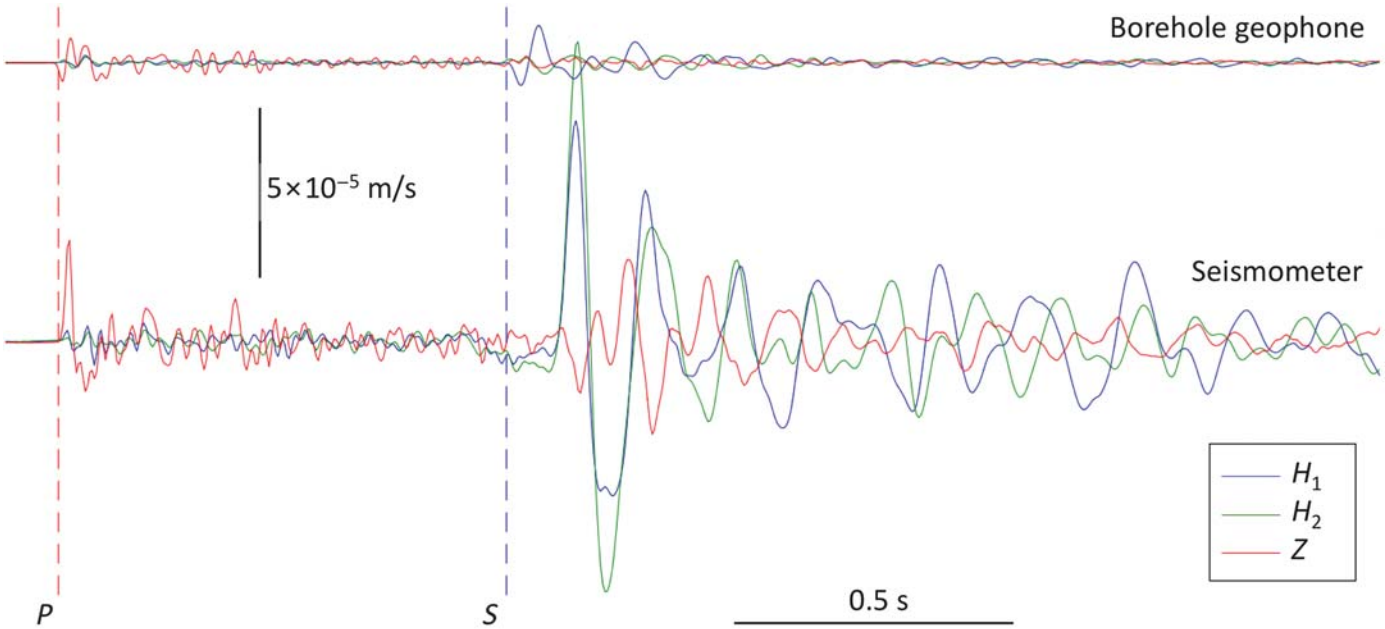

▲ **Figure 2.** Waveform comparison for an M_w 1.76 event recorded on a broadband seismometer and a collocated 3C borehole geophone deployed at 27-m depth. H_1 and H_2 denote the two horizontal components. No rotation into geographic coordinates has been applied, and the orientations of the two horizontal components are different for the geophone and seismometer. A bulk shift has been added to the geophone signals, and the waveforms are aligned on the *P*-wave arrival. The *S*-wave time delay for the seismometer results from propagation through 27 m of near-surface material; the *S*-wave ghost (downgoing reflection from the free surface) is evident in the geophone waveform at approximately twice this time delay. Waveform and polarity differences between the geophone and seismometer reflect differences in instrument and site response, as well as attenuation characteristics of the medium (see the Data Acquisition section for details).

The geophone data were recorded for a total of 35 days; during this time, data were stored on GSX wireless recording boxes. After the survey was completed, the data were harvested from the boxes and formatted into 60 s SEG2 files, totalling 3.5 TB. At each station, a sledge hammer source was used at three different azimuths from the borehole collar, to provide calibration data to determine the orientations of the horizontal components of 3C geophones at 27 m. (Shallower sensors were vertical geophones that did not require such orientation.) Likewise, data from the broadband seismometers and accelerometer were harvested at the end of acquisition program and formatted as 1-hr miniSEED files, totalling 50 GB. Each recording box was equipped with Global Positioning System. This allowed the surface location of each station to be averaged over the span of the program, providing an estimated absolute location accuracy of ± 1 m.

At six of the stations, broadband seismometers and shallow geophone arrays were collocated, which allowed for direct comparison of the two types of sensors. Figure 2 compares waveform characteristics of the *P*- and *S*-wave arrival from an M_w 1.76 induced event, recorded by a 3C geophone at 27-m depth and an overlying near-surface broadband seismometer. No filtering has been applied to these signals, apart from an instrument-response correction to convert the signals to units of velocity (Eaton, 2018). A bulk shift has been applied to the geophone traces to facilitate visual comparison. The geophone signals have opposite polarity to the seismometers due to the polarity standards used by the hydrocarbon industry (Thigpen *et al.*, 1975). As expected, for this event, the geophone waveforms have lower amplitude than the waveforms recorded by the broadband seismometers; this is largely due to the high-frequency response characteristics of the 10-Hz geophones used in this study, which are well suited to characterize events with lower magnitude but do not adequately capture the spectrum of radiated energy above about M_w 1.0 (Urbancic and Wuestefeld, 2013; Eaton and Maghsoudi, 2015). For both types of sensors, the *P*-wave arrival is discernibly enriched in relatively higher frequency signals than the *S*-wave arrival, most likely because of higher *S*-wave attenuation along the path from the source to receiver. In the case of the geophone recording, the loss of higher frequency signals also means that the *S*–*P* amplitude ratio is reduced compared with the seismometer. In both cases, the coda signals following the *P*- and *S*-wave first arrivals contain multiply scattered waves within the sedimentary sequence. The seismometer waveforms are more strongly influenced by near-surface heterogeneity and the free-surface effect (Eaton, 1989) than the buried and cemented geophones. For example, in the case of the geophone waveforms, the *S*-wave surface ghost reflection lags the *S*-wave direct arrival (Fig. 2) but is embedded into the seismometer *S* waveforms because of the close proximity of the sensor to the surface.

Figure 3 shows 3C waveforms for a high signal-to-noise ratio (SNR) event that was recorded by all but one of the shallow wellbore geophone arrays (station 54 was not live at the

Downloaded from https://pubs.geoscienceworld.org/ssa/srl/article-pdf/89/5/1641/4317066/srl-2018055.1.pdf
by Univ Calgary Library user
on 09 November 2018

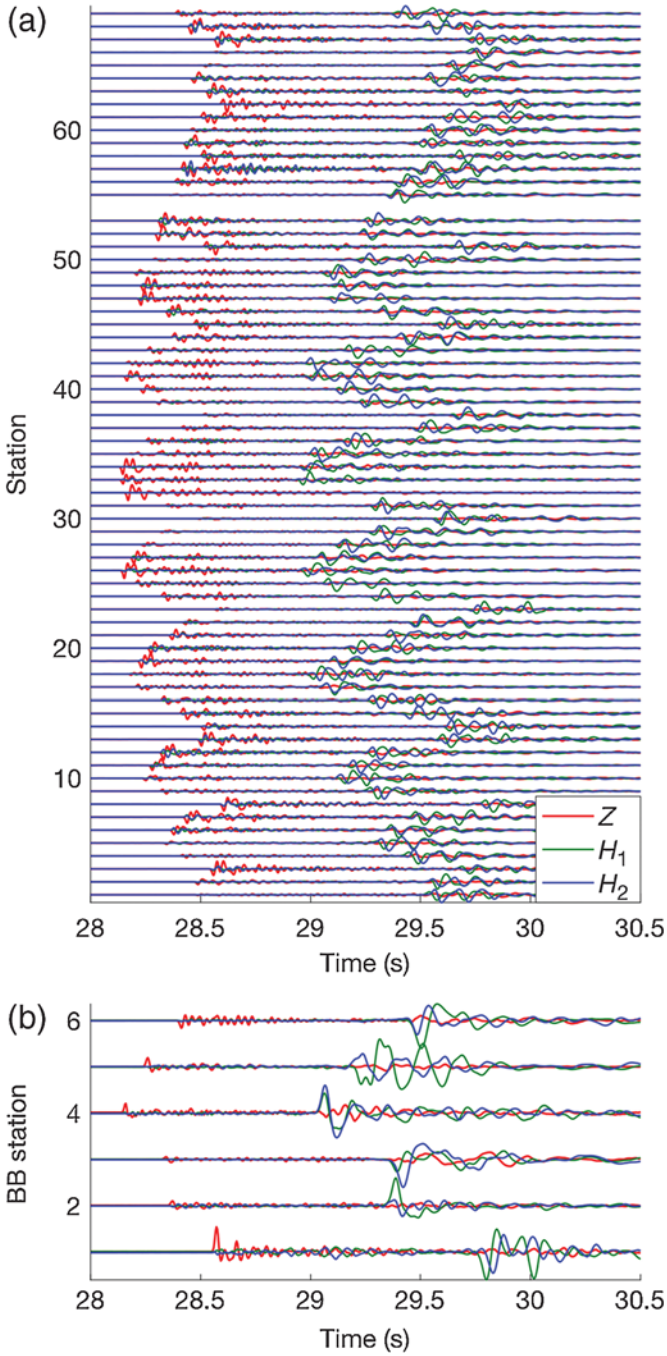

▲ **Figure 3.** Example of a high signal-to-noise ratio event that was recorded across the entire array with (a) 3C geophones (27-m depth) from the 68-station array plus an additional surface geophone and (b) six shallow-buried broadband (BB) seismometers, numbered sequentially.

time of this event) and the six broadband sensors. Geophone station 69 represents a surface 3C geophone. The stations were accessed along east–west trails in the boreal forest and the station numbers reflect the sequential order in which they were accessed. Because this event was well recorded over the entire array, a precise event location could be determined. A number of geophone stations show weak or nonexistent *P*-wave arrival, indicative of the presence of a nodal plane in the source radiation pattern. As discussed later, observations of nodal planes, along with well-characterized *P*-wave polarity measurements, facilitate robust determination of source mechanisms.

DATA PROCESSING

The first step in the data-processing workflow is event detection. During the initial pass, an amplitude-envelope method was used based on the stack of the amplitude envelope of the 3C geophone traces. As part of this process, band-pass filtering was applied to the data (15–70 Hz). Next, the amplitude envelope (Taner *et al.*, 1979) was calculated for all 3Cs and combined into a single amplitude envelope using the following expression:

$$A = \sqrt{H_1^2 + H_2^2 + Z^2}\,. \tag{1}$$

Then amplitude-envelope waveforms for the entire 68-station array were stacked. A threshold was then applied to distinguish events from noise. Using this simple method, > 14, 000 candidate events were detected. This initial set of detections was used to assess the performance of the subsequent method in terms of completeness.

The candidate events were then visually inspected. Fifteen candidate events with high SNR were selected to be used as templates, for application of matched filtering (MF) using the method described by Caffagni *et al.* (2016). Selection criteria for the template events included (a) discernible differences in differential *P*- and *S*-arrival time and moveout, indicative of distinct source locations across the array, and (b) impulsive waveform character with high SNR. The latter criterion meant that the highest magnitude events were not chosen as templates because these events are typically characterized by long coda signals, and in some cases, clipped waveforms. Nevertheless, all 17 of the high-magnitude events detected by the regional network were detected using the MF approach. Following Caffagni *et al.* (2016), the MF detection criterion was based on a summed, multicomponent cross-correlation function, normalized in this study over all of the traces such that the upper limit is unity. An optimal value of the detection parameter was obtained by extensive testing, with an emphasis on avoiding missed detections in comparison with the first-pass detection method described above. This process resulted in a choice of a normalized, summed multicomponent value of 0.025 as the detection parameter.

The application of MF using the 15 template events with this detection parameter resulted in more than 25,000 putative events, which were separated into 15 families based on the template used. A rigorous quality-control (QC) procedure was then applied, in which each of the detected events was visually examined to ensure that both *P* and *S* arrivals could be clearly discerned on at least five stations in the array. This QC procedure resulted in the selection of 4083 events for processing to determine magnitudes and hypocenter locations, as summarized in Figure 4. Ⓔ Table S1 (available in the electronic

Downloaded from https://pubs.geoscienceworld.org/ssa/srl/article-pdf/89/5/1641/4317066/srl-2018055.1.pdf
by Univ Calgary Library user
on 09 November 2018

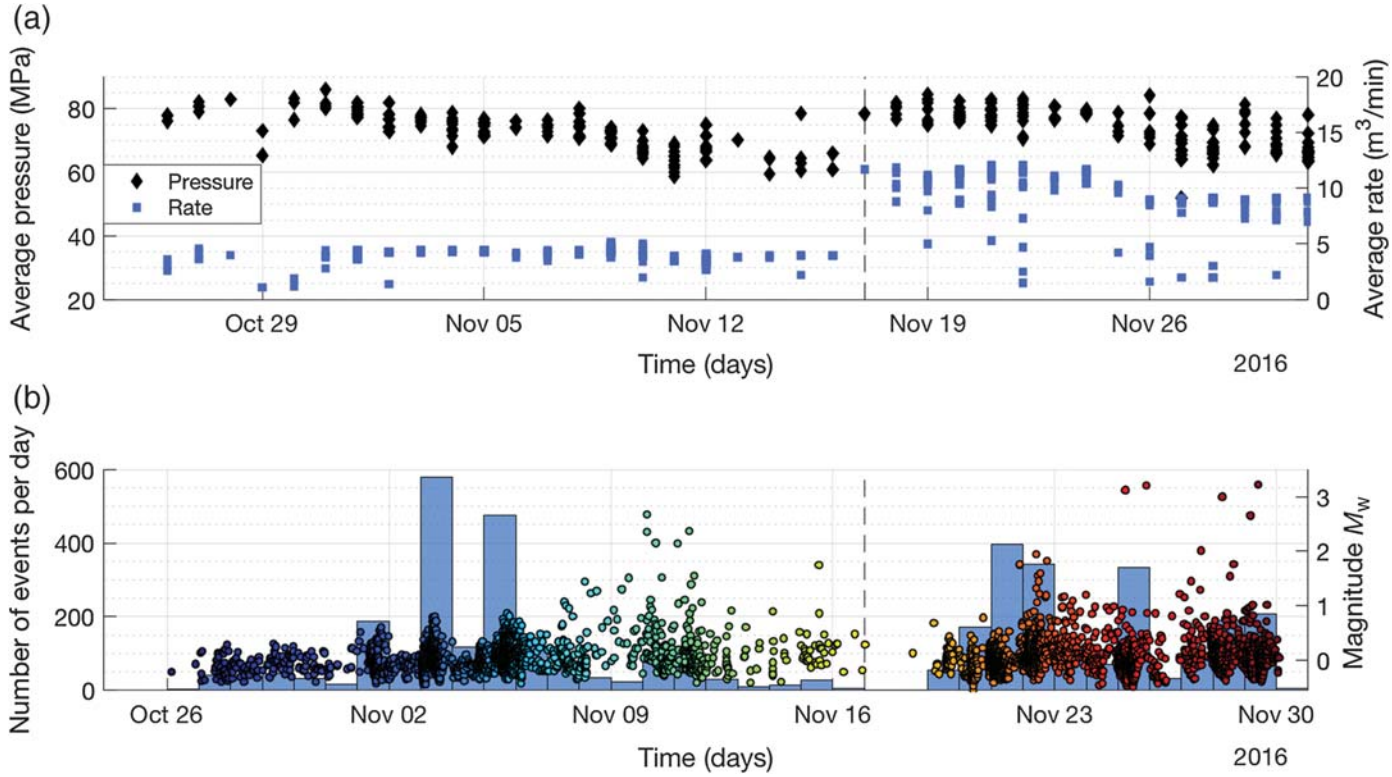

▲ **Figure 4.** Time sequence showing treatment data and seismicity. (a) Average surface injection pressure (black diamonds) and injection rate (blue squares) for each HF stage during the four-well treatment program in 2016. A change in treatment parameters to a higher injection rate is marked by the vertical dashed line. (b) Histogram of the number of events per day and event magnitudes. Events are plotted as circles, with color indicating date of occurrence as shown in Figure 6. Although a large number of events occurred on 3 and 5 November, no event exceeded M_w 2.0 until 10 November. Before this, the magnitude distribution contained abundant of events below magnitude 1.0, with periods of repetition of similar magnitudes. After 10 November, a series of distinct seismicity sequences occurred.

supplement to this article) provides a catalog of the hypocentral parameters and magnitudes of these events.

To determine hypocenter locations, a layered (1D) blocked *P*-wave velocity model was constructed using sonic-log data from a nearby well. An *S*-wave velocity model was derived from the *P*-wave model based on V_P/V_S velocity ratios obtained from correlation of reflections on a collocated multicomponent seismic dataset (Weir *et al.*, 2018). Data from the shallow wells in the array were also used to obtain estimates for *P*- and *S*-wave velocity in the near surface to apply statics corrections (Cary and Eaton, 1993), which account for spatially varying propagation delays in the near-surface layers and adjust the measurements to a horizontal datum. Although perforation shots (shaped-explosive charges that are used to penetrate the wellbore casing to allow egress of fracturing fluids) were used during the HF treatment program, signals from the perforation-shot time windows extracted from the continuous data were weak and generally below the noise level. Thus, because of the poor visibility and unreliable time picks, perforation shots were not used for velocity-model calibration in this study, as is commonly the case for microseismic monitoring (Eaton, 2018).

The initial easting and northing locations of the template events were determined using a simple approach by interpolating the *P*-wave arrival times to find the minimum time, which was assumed to correspond with the epicenter (i.e., vertically above the event). This method involved fitting a hyperboloid function to the *P*-wave arrival times, where the spatial location of the apex determines the event epicenter. Bootstrap resampling with 1000 iterations provided a 95% confidence limit of less than 10 m for location uncertainty of the template epicenters based on the distribution of sensors in this study and the assumed 1D velocity model (see Ⓔ Fig. S1). The final hypocenters for the template events were obtained using a modified direct global search method (Lomax *et al.*, 2014) based on the velocity model derived from available well log data in the vicinity of the geophone array. The initial focal depths of the template events were then refined by comparing the time difference between the *P* and *S* waves to the difference between *P*–*P* and *P*–*S* time in the multicomponent reflection seismic data. For seismic-reflection profiles, the measured times for *P*–*P* reflections (i.e., reflection horizons that are normally considered in seismic exploration) represent a two-way, zero-offset *P*-wave propagation time from the surface to a reflector at depth. On the other hand, horizons observed in *P*–*S* reflection seismic profiles record the sum of the one-way *P* and *S* times at zero offset. Mode-converted *P*–*S* seismic reflections can be recorded using horizontal geophones with conventional reflection seismic sources (Iverson *et al.*, 1989). For correlative

Downloaded from https://pubs.geoscienceworld.org/ssa/srl/article-pdf/89/5/1641/4317066/srl-2018055.1.pdf
by Univ Calgary Library user
on 09 November 2018

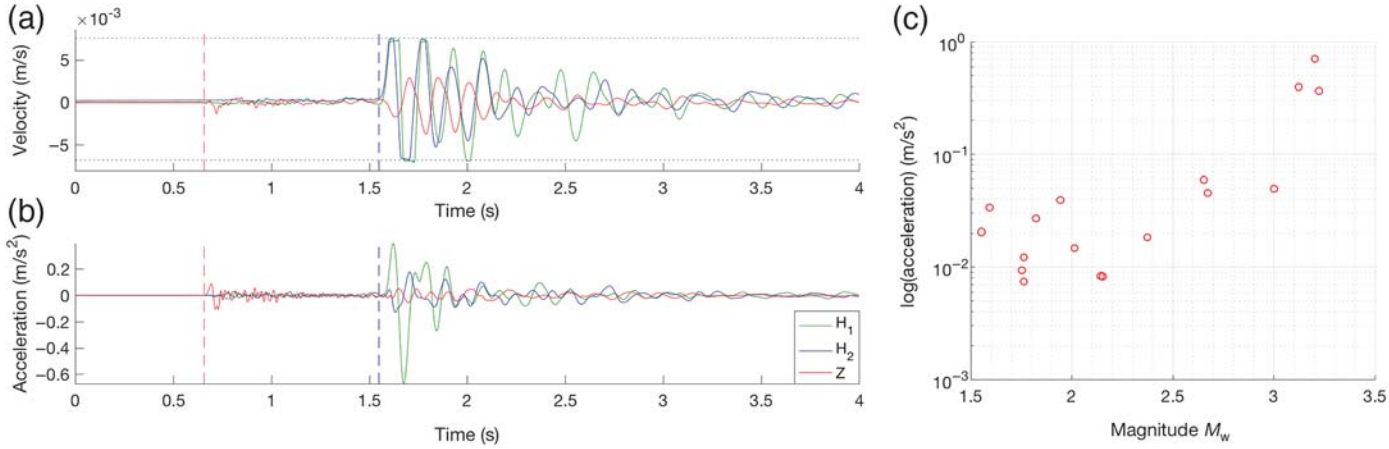

▲ **Figure 5.** Examples of recorded 3C waveforms (H_1, H_2, Z) for an M_w 3.2 event. The vertical dashed red line indicates *P*-wave arrival, and dashed blue line indicates *S*-wave arrival. (a) Broadband seismometer data. Note clipping of the *S*-wave signal, as indicated by the horizontal dotted lines. (b) Waveform recorded by an accelerometer. In this case, there is no clipping of the signal. (c) Peak ground acceleration for the 17 largest induced events during the acquisition program.

horizons, the time difference between *P*–*P* and *P*–*S* reflections is equivalent to the *S*–*P* time for an earthquake, extrapolated to zero offset. After converting the inferred *P*–*P* time to depth, this approach produced adjustments in focal depth of up to about 0.2 km.

Uncertainties in focal depth were estimated by finding the linear interpolation covariance matrix for a plot of squared *P* and *S* times versus squared epicentral distances and taking the error in the *y* intercept, from which the zero-offset *S*–*P* time can be derived. Error propagation was used to convert the uncertainty in time into an uncertainty in focal depth based on the root mean square velocity model, resulting in an average uncertainty in focal depth of 70 m (with a standard deviation of 45 m as shown in Ⓔ Fig. S2).

Relative locations of events that were detected by the MF procedure using template events were determined using an energy-stacking approach with iterative refinement, similar to the approaches described by Roux *et al.* (2014) and Caffagni *et al.* (2016). With this method, hypocenters for MF-detected events were located by searching in a volume in the vicinity of the template event. Hence, time picks were not required to obtain hypocenter locations for MF-detected events. The heart of the method lies in cross-correlation-based alignment and stacking procedure of the waveform data. Based on the location of the template event, as well as a correction term for statics, an arrival-time shift is calculated for each trace and is applied to the data. Then the stack of the amplitude envelope of all the traces is calculated at each grid point. The grid point with the highest maximum amplitude of that stack is chosen as center of the next iteratively refined search grid. Both the *P* and *S* waves were tested separately, and it was found that the *S*-wave stack generally produced clearer and more robust results. Therefore, the vast majority of locations were determined based on the *S* wave. This approach yields precise relative locations of MF-detected events with respect to the corresponding template. Following Zhu and Kanamori (2000), the uncertainty in relative event location can be estimated from the stacking function s using a Taylor expansion around the maximum and omitting higher order terms. For example, the variance σ_x in the spatial x coordinate is given by

$$\sigma_x = \sigma_s \Big/ \left| \frac{\partial^2 s}{\partial x^2} \right|, \tag{2}$$

in which σ_s is the estimated variance in the stack function. This approach leads to an estimated spatial variance in relative hypocenter locations of less than 30 m (see Ⓔ Fig. S3).

Seismic moment magnitudes for all events were estimated by fitting the low-frequency plateau of the *S*-wave displacement spectrum based on the Brune model (Brune, 1970). After applying instrument-response corrections to convert the raw data into units of displacement, the magnitude for each event was determined independently for geophone and broadband recordings by computing the smoothed median unclipped amplitude spectrum over all stations. None of the events clipped on every geophone or every seismometer, and all of the available unclipped signals were used to determine magnitude. In addition, a geometrical-spreading correction was applied based on the hypocentral distance. As shown in Figure 5, for some events, a few of the broadband (as well as geophone) recordings were clipped. Accelerometer recordings are available for all events, of which none are clipped. Based on recorded accelerograms, peak ground acceleration (PGA) for the largest event was ~0.6 m/s^2, or ~6%*g*. The spectral character of the PGA magnitude reported in Figure 5c reflects the source spectrum and (broadband) response of the accelerometer. Three of the events recorded during the ToC2ME program exceed PGA values of 1%*g*, which has been noted to be a threshold for induced-seismicity felt reports in regions of neighboring British Columbia (S. Venables, personal comm., 2018).

The independent magnitude estimates obtained using geophones and broadband seismometers were in good agreement

Downloaded from https://pubs.geoscienceworld.org/ssa/srl/article-pdf/89/5/1641/4317066/srl-2018055.1.pdf
by Univ Calgary Library user
on 09 November 2018

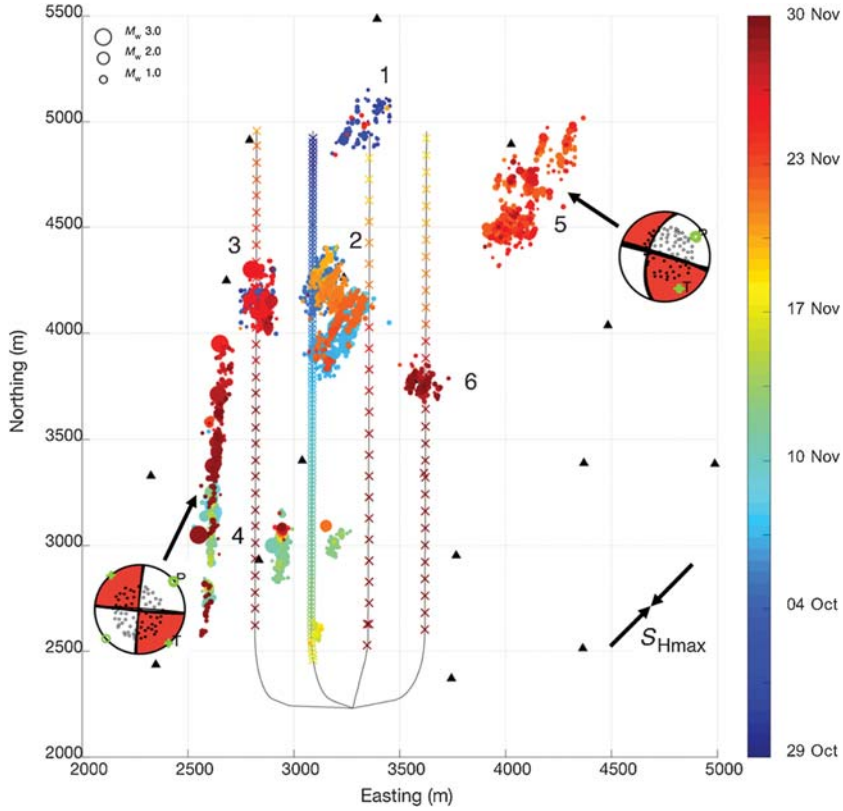

▲ **Figure 6.** Map of event epicenters with clusters labeled. Representative focal mechanisms are also shown, along with orientation of the regional maximum horizontal stress direction (S_{Hmax}). Events are colored by origin time, and crosses along the borehole paths show locations and timing of individual HF stages. Symbol colors use the same scale as in Figure 4b.

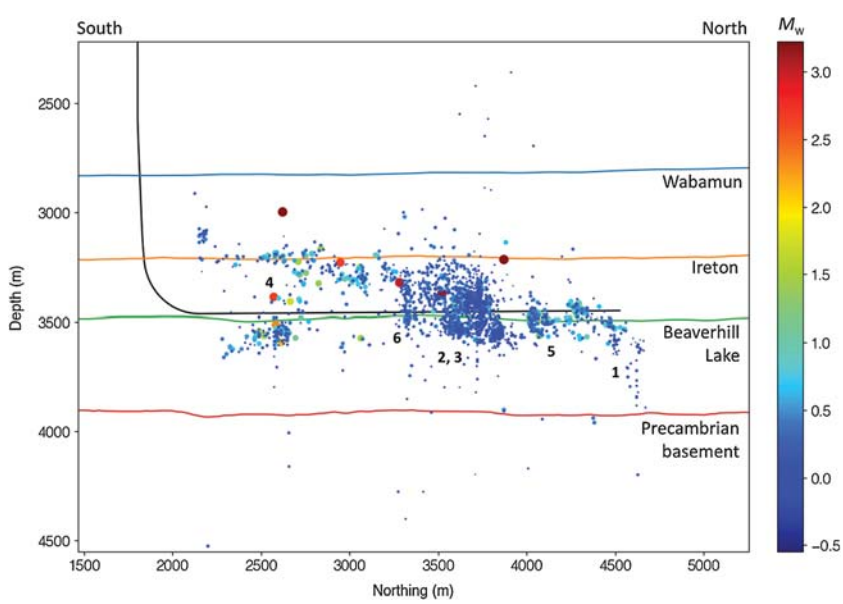

▲ **Figure 7.** South–north vertical section showing treatment wells (curved black line), selected seismically mappable formation tops (see Fig. 9) and event hypocenters, colored and scaled by magnitude. Clusters are numbered as in Figure 6. Many of the events are located at or above the injection zone along the horizontal wellbore. Elevation datum is 910 m above mean sea level.

for events in the range of $0.5 \le M_w \le 1.5$. For larger events, the geophone-derived magnitudes were found to be systematically lower than the magnitudes obtained using broadband sensors, consistent with the reduced geophone amplitudes that are evident in Figure 2. On the other hand, for smaller events, the geophone recordings tended to have higher SNR were found to produce more reliable magnitude estimates. Such systematic differences between magnitudes derived from geophones and broadband sensors, arising from the radiated spectra for events of different magnitude and differences in the frequency response of the instruments, have been previously noted (Urbancic and Wuestefeld, 2013; Eaton and Maghsoudi, 2015). Taking these considerations into account, final magnitudes were computed by taking a weighted average of the geophone and broadband recordings using a cosine taper weighting function with an inflection at $M_w = 1$. The weight for the broadband magnitudes was assigned a value of 1 for $M_w > 1.5$ and a value of 0 for $M_w < 0.5$.

Finally, for a subset of events, focal mechanisms were determined based on the polarity of *P*-wave first motion at the 68 geophone array stations. This analysis is ongoing. Two representative examples of focal mechanisms are presented in Figure 6; these are characterized by predominantly strike-slip fault mechanisms, consistent with previous results for this region (Bao and Eaton, 2016; Wang *et al.*, 2016, 2017; Zhang *et al.*, 2016). Some variability in focal mechanism is observed; for example, whereas events from cluster 4 exhibit nearly pure strike-slip motion on a near-vertical fault plane, events in cluster 5 show apparent oblique slip on a nonvertical fault plane.

INDUCED SEISMICITY SEQUENCES

Figures 6 and 7 summarize the temporal evolution of induced seismicity detected during the ToC2ME program in map view and cross-section view, respectively. Whereas in Figure 6, events are colored based on time of occurrence, in Figure 7, they are colored based on magnitude. The first cluster that was activated, labeled as cluster 1, occurred during HF of the initial treatment well (the second horizontal well from the west). This cluster is composed of several planar features located at the north end of the treatment program. In depth view, these events extend below the injection depth and indicate nearly vertical planar structures.

Downloaded from https://pubs.geoscienceworld.org/ssa/srl/article-pdf/89/5/1641/4317066/srl-2018055.1.pdf
by Univ Calgary Library user
on 09 November 2018

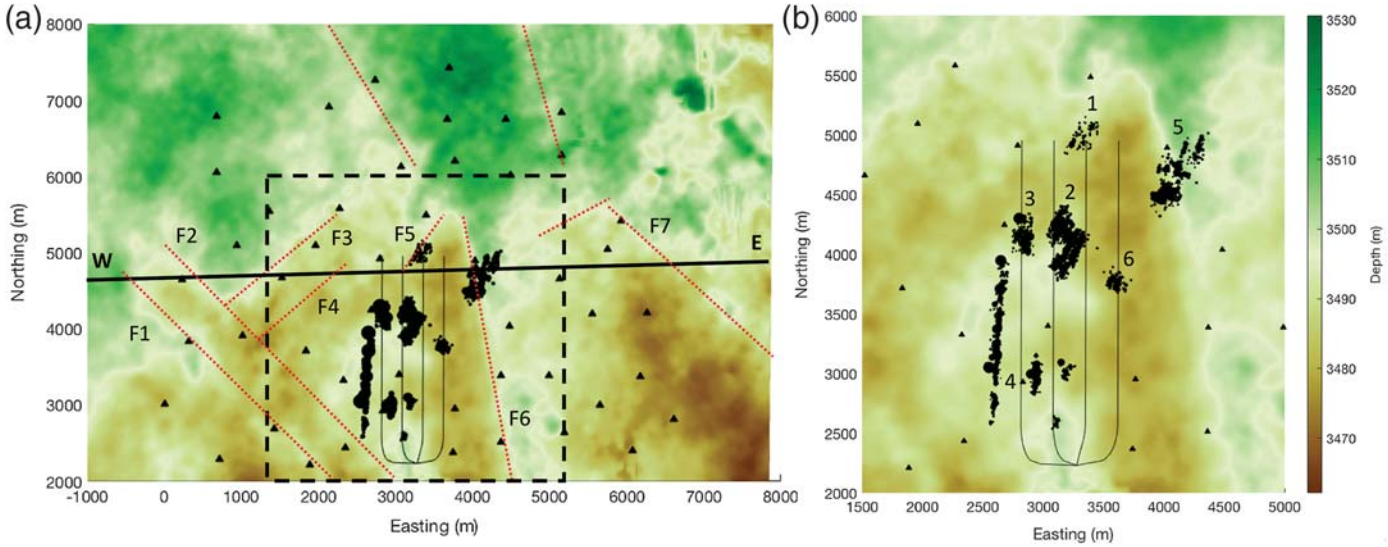

▲ **Figure 8.** Event epicenters overlain on a seismic-derived depth map of the top of the middle to late Devonian Beaverhill Lake Formation, which forms a substrate for the completion zone (Duvernay Formation). Induced events are shown with black circles, and borehole geophone stations are denoted by triangles. (a) Map covering the full west–east extent of available 3D seismic data, showing treatment wells and a number of interpreted faults (red dotted lines). Figure 9 contains a seismic profile along the line marked west–east, showing faults F1–F7. (b) Enlargement of the region enclosed in the dashed box in (a). Interpreted faults are omitted so that their seismic expression (i.e., lateral gradient in the elevation of the stratigraphic surface) can be discerned more easily. Numbers indicate spatial seismicity clusters, as marked in Figure 6.

As the operations continued south along the initial treatment well, cluster 2 was activated. This cluster is composed of a series of northeast–southwest lineaments with an orientation of ~30° E of north. These events are located at or near the depth of the Duvernay Formation, with a consistent spacing of 50–70 m between parallel fault segments. At present, it is not clear if these lineations constitute operationally induced microseismicity (i.e., events associated with hydraulic-fracture growth). If so, the orientation of these lineaments is oblique with respect to the regional S_{Hmax} direction, which is atypical for HF microseismicity (Maxwell, 2014).

For several days after the activation of cluster 2, there was a period of relative quiescence until HF of the initial treatment well reached a position about 500 m from the south end of the horizontal well. Within a period of a few days, a series of north–south linear clusters (3 and 4) was activated, including six events over M_{w} 1.5. The most laterally extensive segment of cluster 4 defines a lineament located several hundred meters west of the treatment wells (Fig. 6), with hypocenters located up to 400 m above the Duvernay Formation (Fig. 7).

Following the completion of the first well, the HF program changed to a series of overlapping completions with higher injection rate in the remaining three wells, including zipper-frac operations for the two eastern horizontal wells. Such operations involve a zipper-like alternating sequence of injection stages between parallel wellbores (Eaton, 2018). During this part of the program, cluster 2 was reactivated along precisely the same lineaments as during completion of the initial well. On 21 November, five events over magnitude 1.5 were recorded. Four of those events were located in cluster 5, northeast of the horizontal wells. Taken together with smaller events in this cluster, the event distribution defined orientations similar to the cluster 2. Following this period of seismicity, cluster 3 was reactivated, this time experiencing two events over magnitude M_{w} 3.0 within 15 hrs. The north–south lineament of cluster 4 was subsequently reactivated, defining an event distribution with a total length of almost 1.5 km. The segments of this cluster that were activated previously were not reactivated despite three additional events over M_{w} 3.0.

DISCUSSION

The availability of 3D multicomponent reflection seismic data provides an opportunity for detailed interpretation of possible relationships between anomalous-induced seismicity and mappable structural features. Prestack inversion of the 3D multicomponent reflection seismic data has been undertaken previously by Weir *et al.* (2018), including a synthetic seismogram well tie that established precise picks for formation tops (horizons). Figure 8 shows an elevation map for the top of the Beaverhill Lake Group, which immediately underlies and forms a substrate for the target horizon, the Duvernay Formation. The Beaverhill Lake horizon is used here as a structural template for the Duvernay because it can be picked automatically with greater reliability throughout the 3D reflection seismic volume.

In parts of the western Canada sedimentary basin, faults with small vertical offsets (a few meters) are often expressed as structural hingelines rather than horizon terminations or discernible offsets (Eaton *et al.*, 1999). A number of interpreted structural features of this nature are shown in Figure 8a. These

Downloaded from https://pubs.geoscienceworld.org/ssa/srl/article-pdf/89/5/1641/4317066/srl-2018055.1.pdf
by Univ Calgary Library user
on 09 November 2018

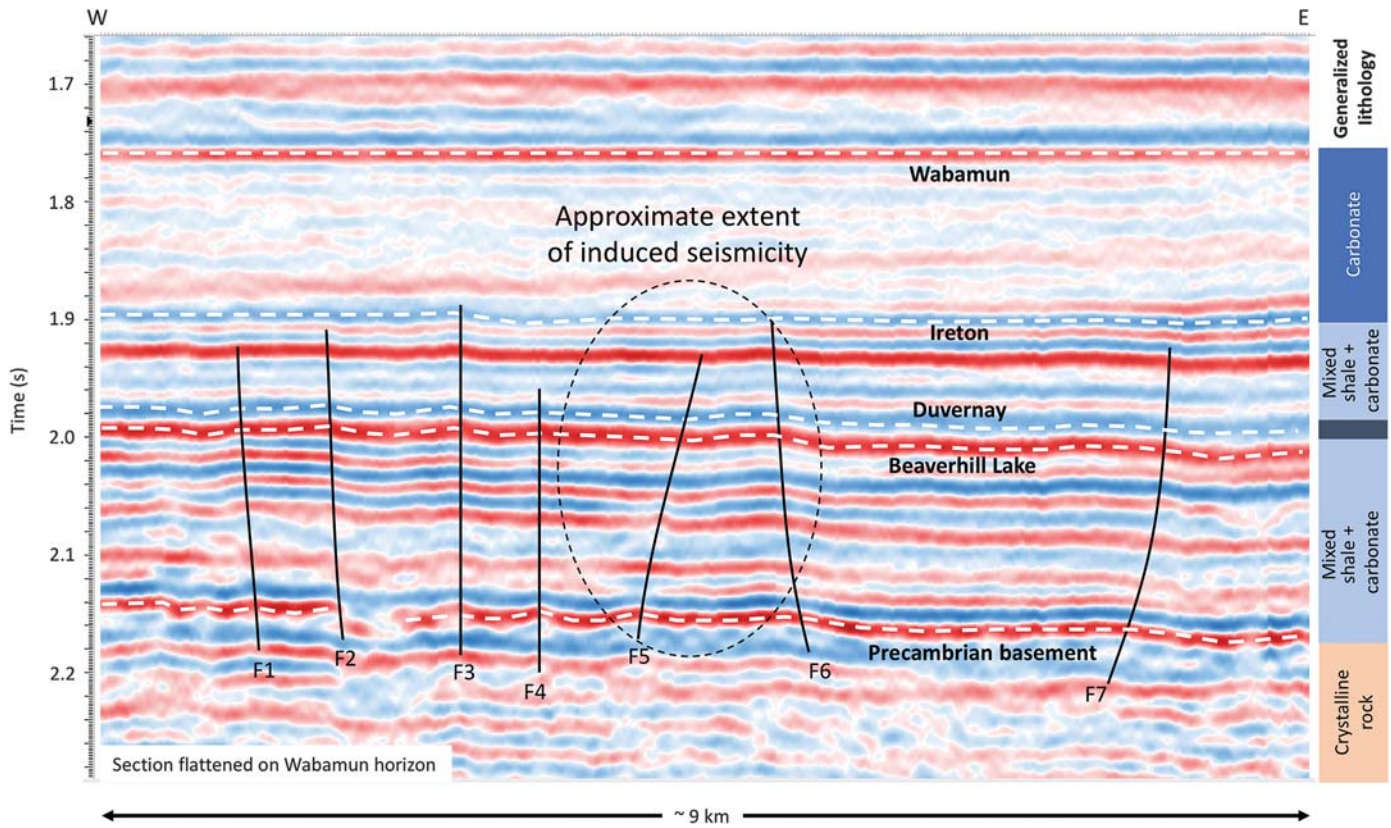

▲ **Figure 9.** Seismic cross section along the east–west profile marked in Figure 8, showing interpreted faults (F1–F7). Red and blue colors indicate positive and negative seismic amplitude values, respectively. True dips are not well resolved in this image because the section is oblique to the intersected faults. The section has been flattened on the top of the Wabamun Formation to accentuate subtle structural features that predate the end of Wabamun deposition. The chart on right indicates generalized lithology within each unit; the dark gray color denotes organic-rich calcareous shale, corresponding to the Duvernay Formation. Faults are interpreted to form a basement-rooted flower structure, extending upward into the lower part of the Wabamun Formation. The dashed ellipse indicates the approximate extent of induced seismicity (Fig. 7), projected into the seismic profile.

features correspond to elongate zones with disruption to the Beaverhill Lake and Precambrian basement. The faults that are indicated (F1–F7) are shown as illustrative aids and are not intended to be comprehensive (i.e., not all zones with similar gradient are marked, to avoid clutter). For comparison, Figure 8b shows an enlargement of a portion of the data without any fault interpretation.

Several small faults (F3 and F5) form the northern edge for an ~20 m down-to-the-north step in the top of the Beaverhill Lake horizon. These features intersect a series of north-northwest–south-southeast-trending linear features labeled as F6 in Figure 8a. Collectively, these features are interpreted to define a structural corridor that is associated with elevated geological susceptibility to induced seismicity (Schultz *et al.*, 2016, 2018; Pawley *et al.*, 2018). Using a similar approach based on the interpretation of curvature anomalies computed for the Precambrian basement seismic horizon, Chopra *et al.* (2017) and Ekpo *et al.* (2018) interpreted this structural corridor as a regional flower structure overlying a strike-slip fault system within the Precambrian basement. Similarly, ideas supporting a basement-rooted flower structure have been discussed at a regional scale from statistical inferences (Schultz *et al.*, 2016) and from sedimentological considerations (Corlett *et al.*, 2018). Simply put, a flower structure is a system of upward diverging conjugate faults with minor dip-slip offsets, which develops above strike-slip faults in transpressional or transtensional tectonic settings (Harding, 1985).

The vertical extent of the interpreted faults is shown in Figure 9, which displays a west–east reflection seismic profile that transects the northern part of the completion program. In the study region, the Late Devonian Wabamun Group is composed of massive limestone and dolostone with a net thickness of ~240 m (Stoakes, 1992). The Wabamun, which represents an overall regressive sequence punctuated by several important transgressive pulses (Halbertsma *et al.*, 1994), is underlain by the Ireton Formation, which is composed of interbedded shale and carbonate with an upper unit of calcareous shale and argillaceous limestone (Switzer *et al.*, 1994). The Duvernay Formation is an organic-rich carbonaceous shale that comprises the source rock for a number of conventional oil and gas systems in Alberta (Switzer *et al.*, 1994). Figure 9 is flattened on the Wabamun horizon to remove any effects of imperfect near-surface statics corrections in the reflection seismic data and to highlight subtle structural features relative to the top of the Wabamun.

Downloaded from https://pubs.geoscienceworld.org/ssa/srl/article-pdf/89/5/1641/4317066/srl-2018055.1.pdf
by Univ Calgary Library user
on 09 November 2018

As evident in Figure 8b, there is little evidence for direct spatial correlation between induced seismicity epicenters and structural features (hingelines) at the top of the Beaverhill Lake horizon. There is, however, some evidence for indirect correlation. For example, cluster 4, defined by a prominent north–south lineament, appears to be bounded by localized higher areas at the top of the Beaverhill Lake (denoted by brown shades). Several other clusters abut the edges of the high-standing patches of the Beaverhill Lake reflection. Taken together, these relationships emphasize the challenges of delineating potential seismogenic structures based on seismic geometry alone, but they also suggest that subtle structural controls may nevertheless be inferred.

Figure 9 shows that inferred basement faults appear to extend upward into the sedimentary section, as high as the lower part of the Wabamun Formation. It should be cautioned, however, that attitudes of the features plotted in Figure 9 reflect apparent dips because the seismic section has vertical exaggeration and is not perpendicular to the strike of these features. This interpretation indicates that the vertical extent of faults imaged by reflection seismic data is consistent with the observation of induced events above the Duvernay zone.

Finally, the QC process used in this study suggests that there may be a plethora of potentially locatable events in the ToC2ME dataset that are not currently included in the catalog. Based on observed low-waveform amplitudes and SNR, the vast majority of events that are not included in the catalog appear to be characterized by magnitudes below M_w 0.5. Most of these may represent low-magnitude operationally induced microseismic events that normally occur during HF operations (Maxwell, 2014; Eaton, 2018). Ongoing analysis of the ToC2ME data is focused on the application of additional templates and other methods such as the source-scanning algorithm (Kao and Shan, 2004) as a way to search for additional events in this dataset.

CONCLUSIONS

This article describes processing and initial interpretation of continuous passive seismic data from the ToC2ME acquired during Fall 2016. The ToC2ME dataset, along with a collocated multicomponent 3C seismic survey, represents the core for a suite of coordinated academic research programs. Induced seismicity event clusters discussed in this article include (1) a set of events above the treatment zone with magnitudes up to M_w 3.2, defining a distinct set of north–south-trending lineaments in the southwest part of the program; (2) a dense cluster of microseismicity in the central part of the program, defining a set of closely spaced lineaments with hypocenters that are at (or near) the Duvernay reservoir zone; (3) a cluster located east of the HF program, at an offset > 500 m from the nearest well; and (4) a cluster at the north end of the program, which delineate planar features extending below the treatment zone. Clusters 2–4 exhibit a general trend of about N30°E, which is about 15° from the expected orientation of S_{Hmax} in this area.

In a broader context, the use of dense sensor arrays in the immediate vicinity of injection operations enables the determination of accurate and precise hypocenters for many seismic events that would otherwise not be detectable using regional networks. The interpretation of observed sequences of small events before and after induced earthquakes is particularly important for elucidating underlying structural relationships and fundamental processes such as the nucleation and arrest of earthquakes induced by HF. Unlike most induced seismicity observed in areas of the U.S. midcontinent, many of the focal depths for these clusters are dominantly at or above the injection zone. Joint interpretation of the distribution of microseismicity with horizons extracted from 3D seismic data indicates a subtle and indirect relationship between induced seismicity clusters and structural features that are discernible from the reflection seismic data.

DATA AND RESOURCES

The seismicity catalog used to prepare the figures in this article is provided as Ⓔ Table S1 (available in the electronic supplement to this article). Continuous raw data (geophone and broadband recordings, network code TC2ME) are available, following a hold-back period that expires on 1 July 2020, through the Incorporated Research Institutions for Seismology (IRIS) data center at http://ds.iris.edu/mda/5B?timewindow=2016-2017 (last accessed July 2018). Hydraulic-fracturing treatment data shown in Figure 4 are available from the Alberta Energy Regulator (https://www.aer.ca, last accessed July 2018). The 3D multicomponent reflection seismic data used in Figures 8 and 9 are proprietary.

ACKNOWLEDGMENTS

The Tony Creek Dual Microseismic Experiment (ToC2ME) program was enabled by generous support from two companies. Financial support was provided by Chevron and the Natural Sciences and Engineering Research Council of Canada (NSERC) through the NSERC-Chevron Industrial Research Chair in Microseismic System Dynamics. Continuous geophone data were collected by Terra-Sine Resources and recorded under license from Microseismic Inc. for use of the BuriedArray method. Arcis Seismic Solutions is sincerely thanked for providing the 3D multicomponent seismic data used in this analysis. Compagnie Générale de Géophysique (CGG) is thanked for providing GeoSoftware used to display and interpret the seismic data. The times and magnitudes of the references events are from the Transportable Array (TA) regional seismic catalog maintained by Nanometrics Ltd. All sponsors of the Microseismic Industry Consortium are also sincerely thanked for their ongoing support of this initiative.

REFERENCES

Atkinson, G. M., D. W. Eaton, H. Ghofrani, D. Walker, B. Cheadle, R. Schultz, R. Shcherbakov, K. Tiampo, Y. J. Gu, R. M. Harrington, *et al.* (2016). Hydraulic fracturing and seismicity in the western Canada sedimentary basin, *Seismol. Res. Lett.* **87,** no. 3, 631–647.

Downloaded from https://pubs.geoscienceworld.org/ssa/srl/article-pdf/89/5/1641/4317066/srl-2018055.1.pdf
by Univ Calgary Library user
on 09 November 2018

Bao, X., and D. W. Eaton (2016). Fault activation by hydraulic fracturing in western Canada, *Science* **354,** no. 6318, 1406–1409.

Brune, J. N. (1970). Tectonic stress and the spectra of seismic shear waves from earthquakes, *J. Geophys. Res.* **75,** no. 26, 4997–5009.

Caffagni, E., D. W. Eaton, J. P. Jones, and M. Van der Baan (2016). Detection and analysis of microseismic events using a Matched Filtering Algorithm (MFA), *Geophys. J. Int.* **206,** no. 1, 644–658.

Cary, P. W., and D. W. Eaton (1993). A simple method for resolving large converted-wave (*P-SV*) statics, *Geophysics* **58,** no. 3, 429–433.

Chopra, S., R. K. Sharma, A. K. Ray, H. Nemati, R. Morin, B. Schulte, and D. D'Amico (2017). Seismic reservoir characterization of Duvernay shale with quantitative interpretation and induced seismicity considerations—A case study, *Interpretation* **5,** no. 2, T185–T197.

Corlett, H., R. Schultz, P. Branscombe, T. Hauck, K. Haug, K. MacCormack, and T. Shipman (2018). Subsurface faults inferred from reflection seismic, earthquakes, and sedimentological relationships: Implications for induced seismicity in Alberta, Canada, *Mar. Pet. Geol.* **93,** 135–144.

Duncan, P. M., and L. Eisner (2010). Reservoir characterization using surface microseismic monitoring, *Geophysics* **75,** no. 5, 139–146.

Eaton, D. W. (1989). The free surface effect: Implications for amplitude-versus-offset inversion, *Can. J. Explor. Geophys.* **25,** 97–103.

Eaton, D. W. (2018). *Passive Seismic Monitoring of Induced Seismicity: Fundamental Principles and Application to Energy Technologies*, Cambridge University Press, Cambridge, United Kingdom.

Eaton, D. W., and S. Maghsoudi (2015). 2b... or not 2b? Interpreting magnitude distributions from microseismic catalogs, *First Break* **33,** no. 10, 79–86.

Eaton, D. W, G. M. Ross, and J. Hope (1999). The rise and fall of a cratonic arch: A regional seismic perspective on the Peace River Arch, Alberta, *Bull. Can. Petrol. Geol.* **47,** no. 4, 346–361.

Economides, M. J., and K. G. Nolte (2000). *Reservoir Stimulation*, Third Ed., Wiley, New York, New York.

Ekpo, E., D. W. Eaton, and R. Weir (2018). Basement tectonics and fault reactivation in Alberta, Canada, in *IntechOpen*, Chap. 4, doi: 10.5772/intechopen.72766.

Halbertsma, H. L, G. D. Mossop, and I. Shetsen (1994). Devonian Wabamun Group of the western Canada sedimentary basin, in *Geological Atlas of the Western Canada Sedimentary Basin*, 203–220.

Harding, T. P. (1985). Seismic characteristics and identification of negative flower structures, positive flower structures, and positive structural inversion, *AAPG Bulletin* **69,** no. 4, 582–600.

Iverson, W. P., B. A. Fahmy, and S. B. Smithson (1989). V_pV_s from mode-converted *P-SV* reflections, *Geophysics* **54,** no. 7, 843–852.

Kao, H., and S.-J. Shan (2004). The source-scanning algorithm: Mapping the distribution of seismic sources in time and space, *Geophys. J. Int.* **157,** no. 2, 589–594.

Lomax, A., A. Michelini, and A. Curtis (2014). Earthquake location, direct, global-search methods, in *Encyclopedia of Complexity and Systems Science*, Springer, 1–33.

Maxwell, S. C. (2014). *Microseismic Imaging of Hydraulic Fracturing: Improved Engineering of Unconventional Shale Reservoirs*, Distinguished Instructor Series, Society of Exploration Geophysicists, Tulsa, Oklahoma.

Pawley, S., R. Schultz, T. Playter, H. Corlett, T. Shipman, S. Lyster, and T. Hauck (2018). The geological susceptibility of induced earthquakes in the Duvernay play, *Geophys. Res. Lett.* **45,** no. 4, 1786–1793.

Roux, P.-F., J. Kostadinovic, T. Bardainne, E. Rebel, M. Chmiel, M. Van Parys, R. Macault, and L. Pignot (2014). Increasing the accuracy of microseismic monitoring using surface patch arrays and a novel processing approach, *First Break* **32,** no. 7, 95–101.

Schultz, R., G. Atkinson, D. W Eaton, Y. J. Gu, and H. Kao (2018). Hydraulic fracturing volume is associated with induced earthquake productivity in the Duvernay play, *Science* **359,** no. 6373, 304–308.

Schultz, R., H. Corlett, K. Haug, K. Kocon, K. MacCormack, V. Stern, and T. Shipman (2016). Linking fossil reefs with earthquakes: Geologic insight to where induced seismicity occurs in Alberta, *Geophys. Res. Lett.* **43,** 2534–2542.

Schultz, R., R. Wang, Y. J. Gu, K. Haug, and G. M. Atkinson (2017). A seismological overview of the induced earthquakes in the Duvernay play near Fox Creek, Alberta, *J. Geophys. Res.* **122,** no. 1, 492–505.

Skoumal, R. J., M. R. Brudzinski, and B. S. Currie (2015). Distinguishing induced seismicity from natural seismicity in Ohio: Demonstrating the utility of waveform template matching, *J. Geophys. Res.* **120,** no. 9, 6284–6296.

Stoakes, F. A. (1992). *Wabamun Megasequence*, Special Publications of SEPM, Broken Arrow, Oklahoma.

Switzer, S. B., W. G. Holland, D. S. Christie, G. C. Graf, A. S. Hedinger, R. J. McAuley, R. A. Wierzbicki, J. J. Packard, and G. D. Mossop (1994). Devonian Woodbend-Winterburn strata of the western Canada sedimentary basin, in *Geological Atlas of the Western Canada Sedimentary Basin*, Canadian Society of Petroleum Geologists and Alberta Research Council, 165–202.

Taner, M. T., F. Koehler, and R. E. Sheriff (1979). Complex seismic trace analysis, *Geophysics* **44,** no. 6, 1041–1063.

Thigpen, B. B., A. E. Dalby, and R. Landrum (1975). Special report of the subcommittee on polarity standards, *Geophysics* **40,** no. 4, 694–699.

Urbancic, T., and A. Wuestefeld (2013). Black box recording of passive seismicity: Pitfalls of not understanding your acquisition instrumentation and its limitations, *Geoconvention 2013*, Calgary, Canada, 6–8 May 2013.

Van der Baan, M., D. W. Eaton, and M. Dusseault (2013). Microseismic monitoring developments in hydraulic fracture stimulation, *ISRM International Conf. for Effective and Sustainable Hydraulic Fracturing*, International Society for Rock Mechanics, 439–466.

Wang, R., Y. J. Gu, R. Schultz, A. Kim, and G. M. Atkinson (2016). Source analysis of a potential hydraulic-fracturing-induced earthquake near Fox Creek, Alberta, *Geophys. Res. Lett.* **43,** 564–573.

Wang, R., Y. J. Gu, R. Schultz, M. Zhang, and A. Kim (2017). Source characteristics and geological implications of the January 2016 induced earthquake swarm near Crooked Lake, Alberta, *Geophys. J. Int.* **210,** no. 2, 979–988.

Warpinski, N. (2009). Microseismic monitoring: Inside and out, *J. Pet. Technol.* **61,** no. 11, 80–85.

Warpinski, N. R., M. J. Mayerhofer, M. C. Vincent, C. L. Cipolla, and E. P. Lolon (2009). Stimulating unconventional reservoirs: Maximizing network growth while optimizing fracture conductivity, *J. Can. Pet. Technol.* **48,** no. 10, 39–51.

Weir, R., D. W. Eaton, L. Lines, D. Lawton, and E. Ekpo (2018). Inversion and interpretation of seismic-derived rock properties in the Duvernay play, *Interpretation* **6,** no. 2, SE1–SE14.

Zhang, H., D. W. Eaton, G. Li, Y. Liu, and R. M. Harrington (2016). Discriminating induced seismicity from natural earthquakes using moment tensors and source spectra, *J. Geophys. Res.* **121,** no. 2, 972–993.

Zhu, L., and H. Kanamori (2000). Moho depth variation in southern California from teleseismic receiver functions, *J. Geophys. Res.* **105,** no. B2, 2969–2980.

David W. Eaton
Nadine Igonin
Andrew Poulin
Ron Weir
Hongliang Zhang
Scott Pellegrino
German Rodriguez
Department of Geoscience
University of Calgary
2500 University Drive NW
Calgary, Alberta
Canada T2N 1N4
eatond@ucalgary.ca

Published Online 11 July 2018

Downloaded from https://pubs.geoscienceworld.org/ssa/srl/article-pdf/89/5/1641/4317066/srl-2018055.1.pdf
by Univ Calgary Library user
on 09 November 2018